Melting Temperature of Metallic Nanoparticles

25

Fan Gao and Zhiyong Gu

Contents

Abstract

Melting temperature is one of the fundamental properties of materials. In principle, the melting temperature of a bulk material is not dependent on its size. However, as the size of a material decreases toward the nanometer size and approaches atomic scale, the melting temperature scales with the material dimensions. The melting temperature of a nanomaterial such as

F. Gao • Z. Gu (✉)

Department of Chemical Engineering, University of Massachusetts Lowell, Lowell, MA, USA
e-mail: Zhiyong_Gu@uml.edu

nanoparticles (isotropic) and nanorods/nanowires (anisotropic) is related to other fundamental physical properties for nanomaterial applications, including catalysts, thermal management materials, electronics materials, and energy materials.

This book chapter focuses on both the theoretical and experimental studies of metallic nanoparticle melting temperature depression. Thermodynamic modeling and molecular dynamic (MD) simulations are discussed regarding the melting behavior of different nanostructures, such as spherical nanoparticles and nanowires. The currently available measurement techniques by using classical differential scanning calorimetry (DSC), recently developed nanocalorimeters, transmission electron microscope (TEM), and optical methods are introduced. In addition, the applications of metal nanoparticles with lower melting temperatures are discussed, such as nanosoldering and sintering for electronics assembly and packaging.

Keywords

Metal nanoparticles • Melting points • Electronics assembly • Flexible electronics

Introduction to Nanoparticle Synthesis

Metallic nanoparticles have extensive applications in catalysis, sensors, electronics, and environmental and biomedical fields. By far, most metallic nanoparticles and their alloys were prepared by either vapor-phase or liquid-phase synthesis, and few started directly from a solid phase. The vapor-phase synthesis methods usually include inert gas condensation, laser ablation, and vapor-liquid-solid (VLS) [1, 2], while the liquid-phase synthesis methods mainly include chemical reduction, microemulsion, electrodeposition, and solvothermal processing [3, 4]. The solid-phase synthesis involves mechanical thermal cycles, such as milling/attrition and reaction between solids [5]. Table 1 summarizes the typical synthetic methods for metallic nanoparticles. Due to the different synthesis methods and growth mechanisms, the shapes of nanoparticles can be classified into the following types: (i) spherical [14]; (ii) polygonal, such as triangle, square, pentagon, hexagon, disk, etc. [15]; (iii) polyhedral, such as tetrahedron, cube, truncated cube, octahedron, etc. [16]; (iv) rodlike, such as nanorod, nanobelt, nanowire, and nanotube [17]; and (v) others, including branched structures (e.g., nanostar) [18] and hollow structures [19]. Figure 1 shows several typical shapes of nanoparticles and nanowires. The metallic nanowires and nanorods have drawn a lot of research interest from the viewpoint of device applications, due to their unique 1D structural property [23]. The main bottom-up synthesis methods of metallic 1D nanostructures include template-assisted electrodeposition, capping agent confined chemical reduction method, nanoparticle self-assembly, vapor-liquid-solid methods, and so on [8].

Table 1 Typical synthetic methods for metallic nanoparticles

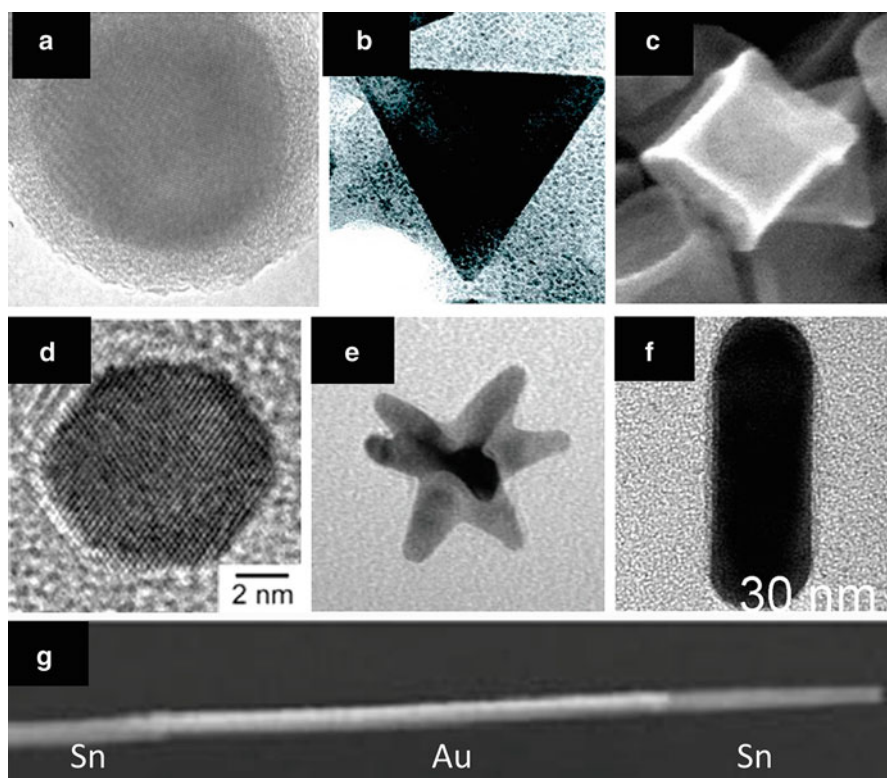|	Synthesis method	Reference
Gas-phase synthesis	Inert gas condensation	[1, 2]
	Laser ablation	[6]
	Vapor-liquid-solid (VLS)	[7]
Liquid-phase synthesis	Chemical reduction method	[8, 9]
	Microemulsion	[10]
	Electrodeposition	[11, 12]
	Solvothermal	[13]
Solid-phase synthesis	Milling/attrition	[5]

Fig. 1 Different shapes of metal nanoparticles. (**a**) Spherical Sn/Ag alloy nanoparticle (Adapted from Ref. [20]); (**b**) gold core-silver shell triangular nanocrystal (Adapted from Ref. [15]); (**c**) palladium nanoparticle cube (Adapted from Ref. [16]); (**d**) Pt octahedron (Adapted from Ref. [21]); (**e**) gold nanostar (Adapted from Ref. [18]); (**f**) gold nanorod (Adapted from Ref. [22]); (**g**) three-segment (Sn-Au-Sn) nanowire (Adapted from Ref. [12]) (Reprinted with permission from American Chemical Society, Copyright (2007), (2009), (2014), (2005), (2012), (2008), (2009), respectively)

For macroscopic (bulk) materials (e.g., size scale larger than one micrometer), the percentage of atoms at the surface is minuscule relative to the total number of atoms of the material; hence, the bulk material should have constant melting point regardless of its size. However, a certain number of physical and chemical properties of nanomaterials, including nanoparticles and nanowires, differ significantly from those at the macroscopic scale due to the high surface area over volume ratio, significant edge effect, and possible appearance of quantum effects at the nanoscale. In this chapter, the size effect on the melting temperature will be discussed.
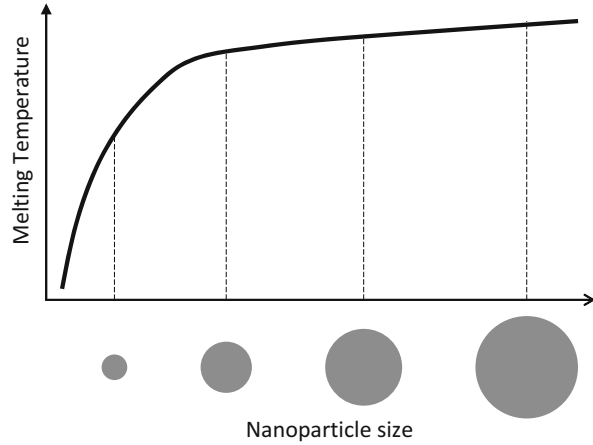
Melting Temperature Depression

Theory

The melting temperature (also referred as melting point or liquidus temperature for alloys) of a solid is the temperature at which it changes state from solid to liquid at atmospheric pressure. At the melting temperature, the solid and liquid phases exist in equilibrium. Studies of melting process and thermodynamic properties of nanoparticles have attracted both the theoretical and experimental interests because of the dramatically different melting behaviors from the bulk materials. In order to better understand the nanoparticle melting behavior, first, let us consider the example of melting for a piece of ice (bulk material) at 1 atmosphere of pressure. When heating up the ice by a constant energy input, the ice will change in three stages, from solid to solid-liquid equilibrium to liquid phases. Before reaching the melting temperature (0 °C), the temperature of the entire piece of ice is kept increasing in the solid state. At 0 °C, the melting temperature, the ice turns to water with absorbing energy, but the temperature of the ice/water mixture does not change till all the ice is changed to the liquid phase. This certain amount of energy required to change from solid state to liquid state (ice to water) at a constant temperature is called a *latent heat of fusion*. The enthalpy change associated with melting is often called as the *enthalpy of fusion*. After that, the temperature of water will keep increasing again under heating. If we "cut" this piece of ice into nanoscale size, the surface-to-volume ratio is much higher than the bulk ice, which dramatically alters its thermodynamic properties. Hence, the melting temperature of nanoscaled ice will melt below 0 °C, and the phenomenon is called *melting temperature depression*.

There is similar phenomenon for the metals and metallic nanomaterials. As the dimensions of a material decrease toward the atomic scale, the melting temperature scales with the material dimension, as shown in Fig. 2. Except few low-melting-temperature (<100 °C) metals, such as gallium and some metal alloys, most bulk metals have very high melting temperatures between one hundred to over one thousand degree Celsius at the atmospheric pressure. However, nanomaterials can melt at a temperature significantly lower than the bulk material. For example, the

Fig. 2 Schematic of size-dependent melting temperature of nanoparticles

melting point of nanometer Au particles (2.5 nm) can be 300° lower than that of the bulk gold [24].

Modeling of the Melting Temperatures

The theoretical model of size-dependent melting temperature of nanoparticles can be simply described by a linear relationship between temperature and the reciprocal of the particle size

$$T_m = T_{bulk}\left(1 - \frac{c}{r_s}\right) \tag{1}$$

where T_m and T_{bulk} are the melting temperatures of nanoparticles and bulk material, respectively, r_s is the radius of particle sphere, and c is a material constant related to material properties, such as material density, surface energy, etc. Figure 3 presents a typical melting temperature depression curve related to the gold nanoparticle size. The dots are experimental data measured from electron diffraction intensities and the solid line is the calculated result [25].

Over the course of the past 100 years, various models have been developed to describe the form of material constant c based on different hypotheses. For an isolated spherical nanoparticle, the Gibbs-Thomson equation was derived for the melting temperature [26]:

$$T_m = T_{bulk}\left(1 - \frac{2\sigma_s}{\Delta H_m \rho_s r_s}\right) \tag{2}$$

Hence, the melting temperature depression (ΔT_m) of a solid nanoparticle can be written as

Fig. 3 Size-dependent melting temperature of gold nanoparticles (Reproduced from Ref. [25]. Reproduced with permission from the American Physical Society, Copyright (1976))
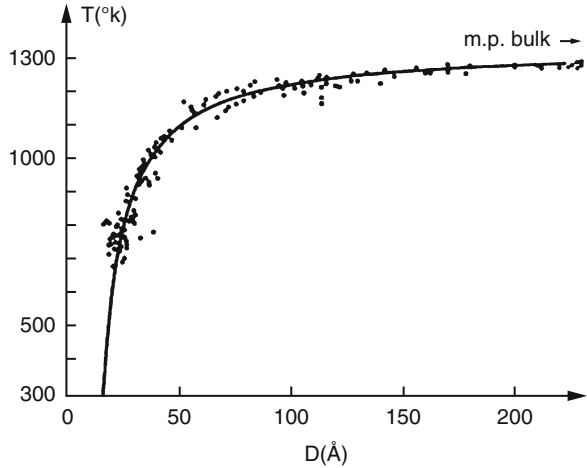
$$\Delta T_m = T_{bulk} - T_m = T_{bulk}\frac{2\sigma_s}{\Delta H_m \rho_s r_s} \tag{3}$$

where σ_s is the surface energy of the solid-liquid interface, ΔH_m is the bulk enthalpy of fusion, and ρ_s is the density of the solid material. This model has been widely used to compare both the experimental data and developed thermodynamic models in melting temperature depression studies [27].

Classically, the melting of small particles has been described by three models: (1) homogeneous liquid-drop model, (2) liquid skin model, and (3) liquid layer and growth model. The general form of the equation is

$$\frac{\Delta T_m(r_s)}{T_{bulk}} = \frac{2\alpha}{\Delta H_m \rho_s r_s} \tag{4}$$

where α is a parameter related to the material interfacial tension between the solid phase and environment [28]. The three models correspond to different expressions for α.

Homogeneous Liquid-Drop Model (LDM)

The earliest thermodynamic model of melting point depression of nanoparticles was developed by Pawlow in 1909 [29]. The liquid-drop model assumes that the entire nanoparticle is under homogeneous phase at both the solid and liquid states, and the phase transition from solid to liquid finishes at a single temperature [30]. The homogeneous liquid-drop model of the size-dependent melting temperature depression is [28, 31, 32]

$$\alpha = \sigma_{sl} - \sigma_{lv}\left(\frac{\rho_s}{\rho_l}\right)^{2/3} \tag{5}$$

where σ_{sl} and σ_{lv} are the surface energy of the solid-liquid and liquid-vapor interface, respectively, and ρ_l is the density of the material in liquid phase. When assuming $\sigma_{lv} = 0$, Eq. (5) is converted to the classical Gibbs-Thomson equation in Eq. (3). Many materials such as In [28], Sn, Pb, and Bi [33] have been studied and compared with liquid-drop model.

Liquid Shell Nucleation (LSN) Model

The liquid shell nucleation model was first originated by Reiss and Wilson, based on the equilibrium of a solid core and a thin liquid shell [32]. This model assumes that the nanoparticle surface starts melting in prior to the core of the solid with a liquid-layer thickness of r_0, so the liquid layer and the surface of the solid coexist till the solid core transforms completely to liquid at the melting temperature [31]. The parameter of the melting temperature depression for the LSN model is derived as

$$\alpha = \frac{\sigma_{sl}}{1 - \dfrac{r_0}{r_s}} + \sigma_{lv}\left(1 - \frac{\rho_s}{\rho_l}\right) \qquad (r_0 < r_s) \tag{6}$$

Several materials have been studied by using the LSN model and consistent results were obtained compared to the experimental values, such as In, [28], Al [34], and GaN [35].

Liquid Nucleation and Growth Model (LNG)

The liquid nucleation and growth model suggests that the nanoparticle surface melts and nucleates initially, and the liquid layer at the surface grows and moves into the solid with the increase of the temperature. The parameter of the melting temperature depression can be given by [31, 36–38]

$$\sigma_{sl} < \alpha < \frac{3}{2}\left(\sigma_{sv} - \sigma_{lv}\frac{\rho_s}{\rho_l}\right) \tag{7}$$

where the ρ_s and ρ_l are the material density of the solid and liquid (some articles use molar volume ν_s and ν_l to represent), which are related to the material densities, $\rho_s = M/\nu_s$ and $\rho_l = M/\nu_l$, with M being the molecular weight [39]); the σ represents the surface energy between solid, liquid, and vapor phases (indexes s, l, and v, respectively). A comparison of the predictions of this theory with experimental results was given in Sn, In, and Au metal nanoparticles [38].

Particle Shape Effect

All the models mentioned above were developed based on the spherical nanoparticles. Due to the different synthesis methods and growth mechanisms, nanoparticles can be controlled in not only spheres but also many other shapes,

such as triangular prisms, hexagonal plates, nanorods, and cubes, as discussed in the section "Nanoparticle Synthesis". Since the theory of the melting temperature depression was built upon the large surface-to-volume ratio of nanostructures, the surface areas of a nanoparticle in different shapes can be varied, even for the nanoparticles with the identical volume, which may result in different melting temperature depressions [33, 40–42].

In general, the equation of the size- and shape-dependent melting temperature depression for anisotropic nanoparticles is similar to Eq. (1), with adding a shape-corrected parameter z [30], and written as

$$T_m = T_{bulk}\left(1 - \frac{c}{zr}\right) \tag{8}$$

The shape parameter z equals to 1, 1.5, and 3 for sphere nanoparticles, nanowires, and thin films, respectively.

A melting temperature model for nanowires or nanorods with diameter d and length h was derived by Sar et al. [42],

$$T_m = T_{bulk}\left[1 - \frac{\sigma_{sv} - \sigma_{lv}}{H_m\rho_s}\left(\frac{4}{d} + \frac{2}{h}\right)\right] \tag{9}$$

A shape factor, α, is introduced into the model to describe the different shapes of the nanoparticles [33, 43], as shown in the following equation:

$$\alpha = \frac{S'}{S} \tag{10}$$

where S and S' are the surface areas of the spherical and other shaped nanoparticles in the same volume. Therefore, the surface area of any shape nanoparticle can be computed as

$$S' = \alpha S = 4\alpha\pi R^2 \tag{11}$$

where R is the spherical particle radius. Combining with the cohesive energy of the nanoparticle, the equation of the melting temperature can be rewritten as

$$T_m = T_{bulk}\left(1 - 6\alpha\frac{r}{D}\right) \tag{12}$$

where $D = 2R$ and r is the atomic radius. This is the general equation for the size- and shape-dependent melting temperature of nanoparticles. It is also found that the shape effect on the melting temperature increases when particle size is decreased [33].

In addition, the models for the one-dimensional nanostructures such as nanowires and two-dimensional thin films need to be modified. Lu et al. discussed the size-, shape-, and dimensionality-dependent melting temperature and found that the

melting temperature decreases with a decrease of the nanocrystal dimensions [41]. When the nanoparticle size is large enough, the melting temperature depression possesses the relationship as

$$\Delta T_m(D, \text{ thin films}): \Delta T_m(D, \text{ nanowires}): \Delta T_m(D, \text{ nanoparticles}) \approx 1$$
$$: 2\lambda_{wire} : 3\lambda_{particle} \tag{13}$$

where D is the nanoparticle size and λ is the shape factor defined as

$$\lambda = \left(\frac{A_2}{A_1}\right)\left(\frac{V_1}{V_2}\right) \tag{14}$$

where the subscripts 1 and 2 denote the nanostructure with typical shape (e.g., spherical nanoparticle and cylindrical nanowires) and other shapes, A is the surface area, and V presents the volumes of the nanostructures. This model is valid for most of nanocrystals such as Au, Ag, Ni, Ar, Si, Pb, and In [41].

Latent Heat of Fusion

The enthalpy difference, ΔH_m, of nanoparticles would be lower than that of the bulk materials due to the increase in the surface energy, which is a general feature of melting for all nanoparticles.

A derivation of the Gibbs-Thompson equation was developed for the size-dependent heat of fusion:

$$\Delta H_m = \Delta H_{\text{bulk}} - \frac{2\sigma_{sl}}{\rho_s r} \tag{15}$$

where ΔH_m represents the heat of fusion for a nanoparticle with a radius r.

According to the report of Lai et al., the equation of heat of fusion for nanowires is [44]

$$\Delta H_m = \Delta H_0 \left(1 - \frac{2t_0}{D}\right)^n \tag{16}$$

where ΔH_0 is the heat of fusion for bulk material and t_0 is the given thickness of a liquid layer covering the solid core at the melting temperature T_m. The exponent n is 3 for spherical nanoparticles and 2 for nanowires.

Substrate Effect

Although all the models mentioned above were derived based on the free particle hypothesis, almost all the experiments regarding the size-dependent melting

temperature were performed on a solid substrate (not free and isolated particles) or through contact with other materials; however, these experimental results were usually compared to models without considering the effect of the substrate.

Experimentally, Chen et al. observed the phase transition of Ag nanoparticles on graphite and alumina substrates through in situ high-resolution transmission electron microscopy (HRTEM). It is found that the Ag nanoparticle had a direct solid-to-gas transition (evaporation) other than a solid-to-liquid transition (melting) on the graphite substrate. The solid-to-liquid transition only took place on the alumina substrate [45].

Lee et al. developed a theoretical model based on the CALPHAD (Calculation of Phase Diagrams) method to study the effect of the interfaces between the gold nanoparticles and substrates [46]. Instead of using the respective surface tension value of each face, the mean surface tension was introduced. It is found that the calculated results for heterogeneous particles on ceramic substrates (particles on solid substrate) yield almost the same melting temperature as those of homogeneous nanoparticles (free particle without considering the substrate). This result is consistent with Guisbiers et al. who believed that the stresses appeared in the deposited nanoparticles and the substrate-nanoparticle interface tension was negligible [40]; however, the melting temperature of heterogeneous particles on metallic substrate has higher values than the homogeneous ones [46].

Experimental Methods for Measuring Nanoparticle Melting Temperatures

The mathematical models discussed in the last section provide the theoretical support of the size-dependent melting temperature depression for nanomaterials. In order to better understand this phenomenon and accurately obtain the melting temperature information, experimental measurement is imperative and essential, including both the visible observation and energy-associated physical properties.

Differential Scanning Calorimetry (DSC)

DSC is a highly sensitive thermoanalytical technique to investigate the thermodynamic properties (including melting temperature, transition enthalpy, phase transformation, crystallization temperature, degree of crystallinity, glass transition temperature, and specific heat) of materials, such as metals, polymers, and biomacromolecules [47, 48]. DSC measurement determines the temperature and heat flow associated with material transitions as a function of time and temperature [49].

In principal, the melting temperature can be obtained by measuring the relationship between temperature and internal energy, where the solid-to-liquid phase transition occurred. For the material enclosed in a DSC pan, some known energy

E is supplied to the pan by heating, and the temperature T is measured. The direct measurement of the energy and temperature is called *caloric curve*.

$$E = E(T) \tag{17}$$

The *heat capacity* is defined by the relation

$$C_p(T) = \frac{\partial E}{\partial T} \tag{18}$$

which is the partial derivative form of the caloric curve. A calorimeter is an equipment to measure the heat capacity, C_p. A differential calorimeter measures the heat of a sample relative to a reference sample. A DSC measures both the energy change and heat capacity and heats the sample with a linear temperature ramp, and the heat is transferred to the sample and reference pan through the thermoelectric disk.

During a phase transition, a temperature difference between the sample and reference pans can be measured by means of a thermocouple. The heat flow signal is proportional to the difference between sample and reference temperature, determined by the thermal equivalent of the Ohm's law [47]:

$$\dot{q} = \Delta T / R \tag{19}$$

where q is the sample heat flow, ΔT is the temperature difference between the sample and the reference, and R is the resistance of the thermoelectric disk [50].

Due to the availability and operability, DSC is one of the most widely used tools to characterize the thermal properties such as melting temperature and heat of fusion for nanoparticles and nanowires, such as silver, copper, aluminum, zinc, tin, and alloy nanoparticles [17, 51–58]. Figure 4a shows a typical DSC measurement for Sn nanoparticles with the size about 61 nm, indicating that the melting temperature is 230 °C, about 2 °C temperature depression [58]. Figure 4b shows the DSC measurement of Sn nanowires with diameter in 50 nm and length in 5 μm, which shows 0.7 °C melting temperature depression [12].

Nanometer Scale Calorimetry

Conventional DSC measurement as discussed above, while powerful, is usually not sensitive enough for a small amount of sample (e.g., less than 1 mg). This is due to the fact that the amount of heat absorbed is too small to be detected. A scanning nanocalorimetry technique was first developed by Lai et al. for melting temperature study of Sn thin films [59]. In the device, four components in a typical calorimetry system, including the sample, sample holder, heater, and thermometer, were combined into a single multilayer thin-film configuration, as shown in Fig. 5a, b. The nanocalorimeter was placed in a vacuum evaporator system for both the Sn thin-film deposition and calorimetry measurements without breaking the vacuum.
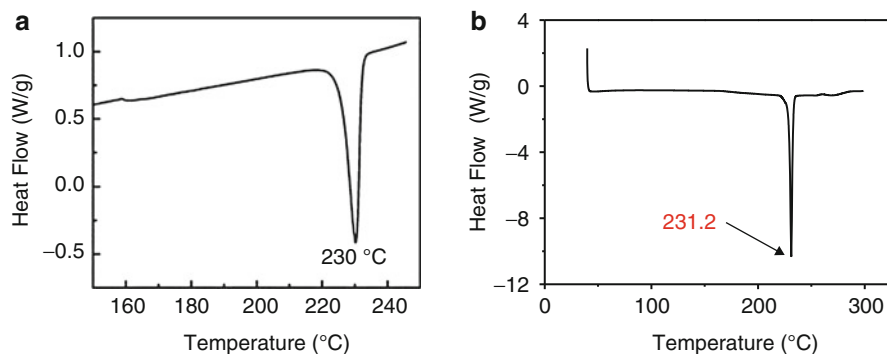
Fig. 4 DSC curve of (**a**) as-synthesized Sn nanoparticles [58] (Reprinted with permission from Elsevier, Copyright (2006)). (**b**) Sn nanowires (Adapted from Ref. [12]. Reprinted with permission from American Chemical Society, Copyright (2009))

Fig. 5 Cross-sectional (**a**) and planar (**b**) view of nanocalorimeter. System is based on reduced thermal mass sample holder made using a silicon nitride membrane which is only 1,800 Å thick and mechanically supported at the perimeter by the Si substrate. A thin-film Ni layer is deposited on the top side of the membrane and severs as both heater and thermometer. The sample of interest is deposited on the bottom side of the membrane (Reproduced from Ref. [59]. Reprinted with permission from American Institute of Physics, Copyright (1995))
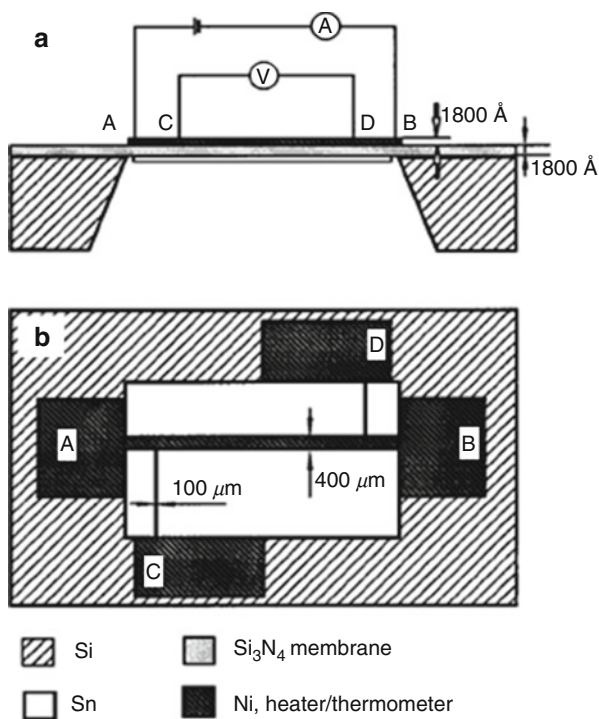
The very low rate of thermal evaporation deposition (~3 Å/s) results in Sn nanoparticles in the size range of 5 ~ 50 nm in radii other than continuous thin film. Hence, the small metal particles can be prepared with high purity and free surfaces to study their melting behavior. The experimental data points of the

Fig. 6 Size dependence of (**a**) the melting points and (**b**) normalized heat of fusion of Sn particles measured by a nanocalorimeter. The *solid line* is from calculated results (Reproduced from Ref. [44]. Reprinted with permission from the American Physical Society, Copyright (1996))
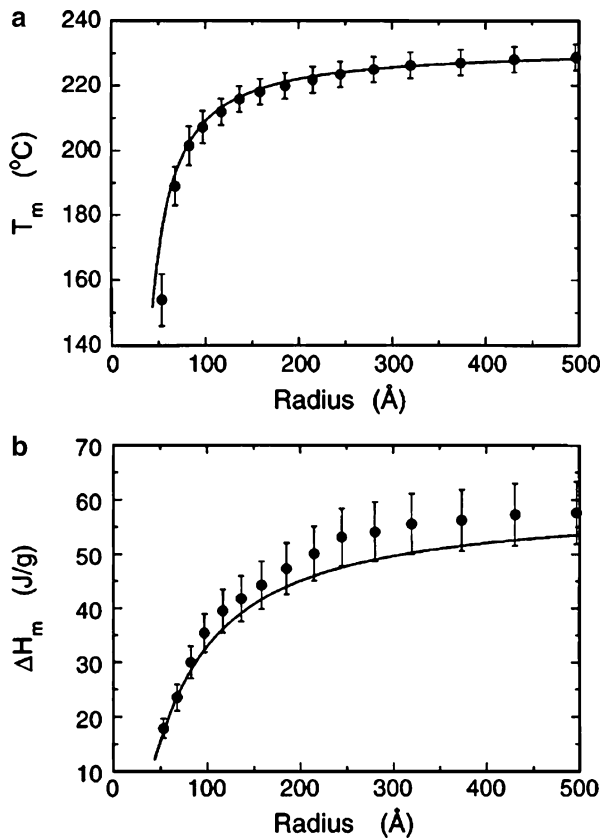
size-dependent melting temperature and normalized heat of fusion of Sn nanoparticles from the nanocalorimeter measurement were shown in Fig. 6 [44]. The melting temperatures were decreased as the size of Sn nanoparticle decreased, and a reduction of 70 °C was measured for Sn nanoparticles with a radius of 50 Å. Meanwhile, the normalized heat of fusion ΔH_m dramatically decreases about as much as 70 % from the bulk value, which is 58.9 J/g. The experimental results from nanocalorimeter are mostly used to compare with mathematical models and computer simulation results for Sn and In nanoparticle system [28, 44].

Schmidt et al. used a nanocalorimeter and reported the measurement of sodium cluster containing 139 atoms, with caloric curve and heat capacity, as shown in Fig. 7. At the melting point, a step in the caloric curve, $U(T)$, is shown, which corresponds to the energy used for phase transition from solid to liquid without a temperature increase. The plot of heat capacity $c(T)$ with a peak indicates the melting temperature of the atomic Na clusters [60]. The melting temperatures of the sodium clusters containing 70 to 200 atoms are on average 120 K (33 %) lower than the bulk material.

Fig. 7 Heat capacity $c(T)$
and its integral, the caloric
curve $U(T)$, for a positively
charged sodium cluster
containing exactly 192 atoms.
The *solid dots* show the
experimental results. From
the maximum of $c(T)$, one
obtains the melting point
T_{melt}, and from the height of
the smoothed out step in the
caloric curve, one gets the
latent heat of fusion q, that is,
the energy necessary to
destroy the crystalline lattice
at the melting point
(Reproduced from Ref. [60].
Reprinted with permission
from Nature Publishing
Group, Copyright (1998))
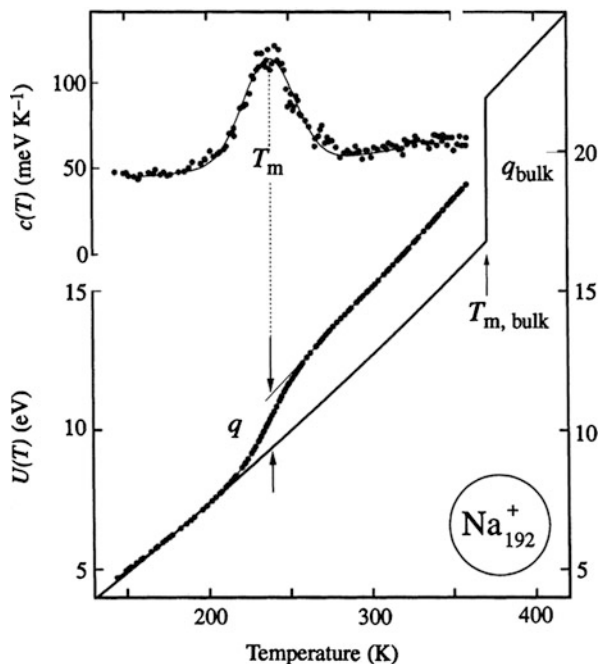
Transmission Electron Microscope (TEM)

TEM is a widely used method to observe the nanoparticle melting phenomenon. This technique has been used to study the melting temperature depression of small metal particles for decades. Takagi is the first researcher to observe the size-dependent melting temperature depression phenomenon by TEM in metal thin films with thickness ranging from 10 Å to 1,000 Å [61]. Due to disordering of crystalline structure of a metal at the liquid phase, the melting temperature was monitored by the loss of crystalline structure with increasing temperature, which can be observed by electron diffraction pattern change. Some early works reported the use of electron diffraction technique to extend the measurements for tin [62, 63] and Au nanoparticles [25] with the size range of 20 ~ 50 Å. The other metal thin films and nanoparticles such as silver, copper, aluminum, lead, indium, and germanium have been studied too [64] [65, 66]. However, this method is only suited to study a set of nanoparticles with identical diameters. Due to the polydispersion of nanocrystals encountered in a specimen, it is generally not possible to observe a sharp change in the ring patterns during the melting process [25].

The in situ TEM and high-resolution TEM (HRTEM) technique could accurately record the single nanoparticle melting process. Chen et al. reported two different phase transitions of a ~8 nm silver nanoparticle on both graphite and alumina substrates through in situ HRTEM observation [45]. For the graphite substrate, silver nanoparticle was heated up to 677 °C and the shrinkage to disappearance of
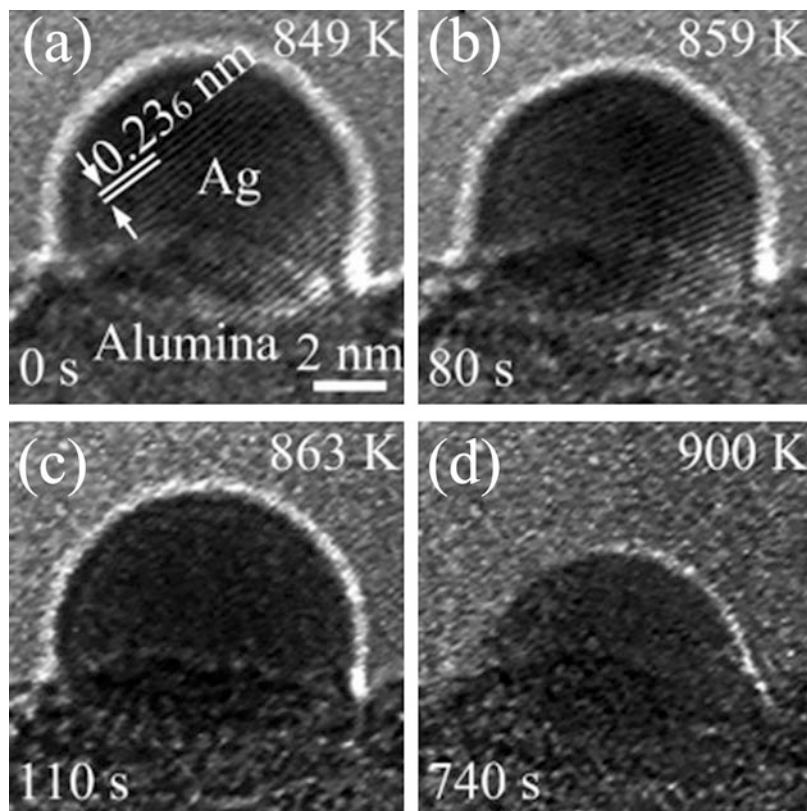
Fig. 8 A series of HRTEM images showing the annealing process of a 8 nm silver nanoparticle on an alumina substrate (Reproduced from Ref. [45]. Reprinted with permission from American Institute of Physics, Copyright (2010))

the particle (crystalline to gas) was observed. However, the silver nanoparticle on an alumina substrate remains the crystal structure at 586 °C and gradually changed into a semispherical particle with uniform contrast, accompanied by the disappearance of the lattice fringes (crystalline-to-liquid transition) during the temperature increase to 590 °C, as shown in Fig. 8. After melting, the silver nanoparticle placed on the alumina substrate shrunk in size due to evaporation. The possible reason for these two-phase transition behaviors is the different solubility limit of metallic aluminum and carbon atoms in liquid silver [45].

In some other cases, the electron beam-induced melting and coalescence of nanoparticle and nanowire under TEM without stage heating were observed [67–69]. Due to the high-energy beam, the nanoparticle will start melting under the electron beam (e-beam) irradiation. The phenomenon of quasi-melting and structural fluctuations in small particle was observed under TEM electron beam [70, 71].

Gao et al. reported the interdiffusion and melting behavior of Cu-Sn two-segment nanowire system (Fig. 9a) under TEM e-beam irradiation. The surface
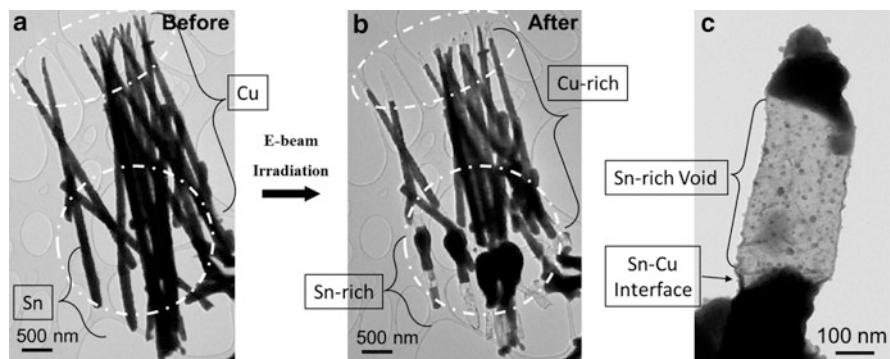
Fig. 9 TEM images showing the shape transformation of Cu-Sn two-segmented nanowires (**a**) before and (**b**) after the e-beam irradiation; (**c**) zoom-in image of void formation in the Sn-rich segment at Sn-Cu interface (Reproduced from Ref. [72])
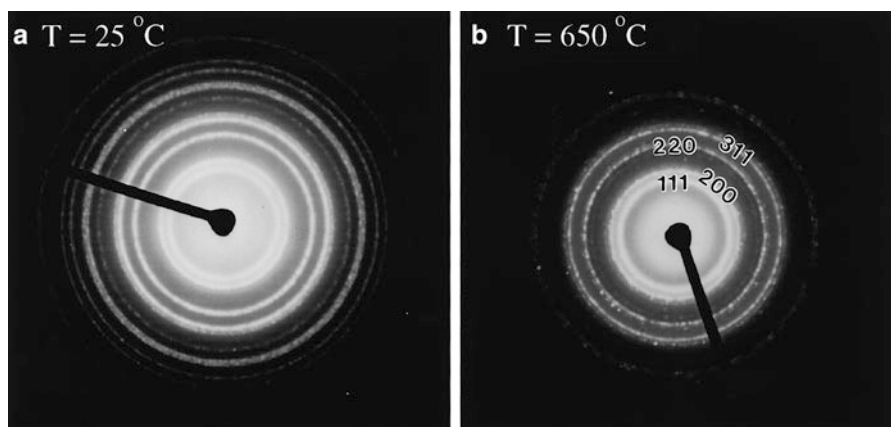

Fig. 10 Diffraction patterns of Pt nanocrystal at (**a**) 25 °C and (**b**) 650 °C (Reproduced from Ref. [73]. Reprinted with permission from American Chemical Society, Copyright (1998))

oxide effectively confined the movement of metallic copper and tin atoms along the one-dimensional nanowire. After the e-beam irradiation, there were Sn-segment melting and interdiffusion between Cu and Sn segments with void formation at Cu-Sn interfaces and also around the tips of the Cu segment, as shown in Fig. 9b, c. The melting of Sn under e-beam irradiation was caused by a temperature rise due to electron thermal spikes in the nanowire and poor thermal conduction [72].

The Pt nanoparticle surface melting and a surface solid-liquid core coexistence have been observed by Wang et al. [73] The electron diffraction change of Pt nanoparticle at 25 °C and 650 °C was recorded, as shown in Fig. 10. The total diffraction intensity was dramatically decreased, indicating the crystallinity vanish of the nanocrystals.

However, as the particle size decreases, the diffraction technique becomes increasingly inaccurate due to line broadening [74]. Moreover, TEM is limited to structural measurement only; it cannot measure the heat associated with the melting process, such as the heat of fusion.

Laser-Induced Method

In section "Nanometer Scale Calorimety", the melting temperature measurement of Na clusters was conducted by a laser-aided method. Laser is a good source to generate enough energy to excite nanoparticles and observe the melting behavior. The basic idea of the laser-induced experiment is using photon energy absorbed by electrons to heat particles, which is due to electron-phonon scattering that occurs in a few picoseconds, and thus their temperature increases [75].

Habenicht et al. used a Nd:YAG laser (wavelength $\lambda = 532$ nm, full width at half maximum of 10 ns) to irradiate gold triangles with side lengths between 400 and 800 nm. After heating with a laser pulse, the metal triangles become molten in the nanosecond duration and then solidify again as a result of the heat loss into the substrate [76, 77]. The resulting solids provide insight into the nanostructures at the moment of solidification. Figure 11 shows that the dewetting process, which appears upon laser-induced melting of nanostructures and leads to a jumping of the droplets off the surface, is used for deposition of nanoparticles onto other non-wetting substrate (glass substrate in Fig. 11b). Through this process, surface energy is transformed into kinetic energy of droplets [77].

In addition, a laser-induced Au nanoparticle melted at 940 °C was reported by Inasawa et al., which is at least 100 °C lower than that of the bulk material [78]. Hodak et al. reported that the Au-Ag core-shell nanoparticles were melted into homogeneous alloyed nanoparticles at a much lower temperature (157 °C) than the expected melting point (825 °C) by picosecond laser-induced heating (at 532 nm) [79].

Optical Methods

Plasmons are electron excitations that occur in metals and semiconductors in response to visible electromagnetic waves, resulting in the collective oscillation of conduction band electrons, whose phenomenon is plasmon resonance [80, 81]. The solid to liquid phase transition (melting) of nanomaterials with certain optical properties could be identified by optical methods such as absorption spectroscopy [82, 83]. For example, it is known that gold nanoparticles interact with visible light due to their distinct interband transition (5d $\rightarrow$ 6sp) and surface plasmon resonance (SPR), which is one of the size-dependent properties [78].

The SPR effect on size-dependent melting of Cu nanoparticle embedded in a silica matrix was studied by Yeshchenko et al. [84]. Figure 12 depicts the
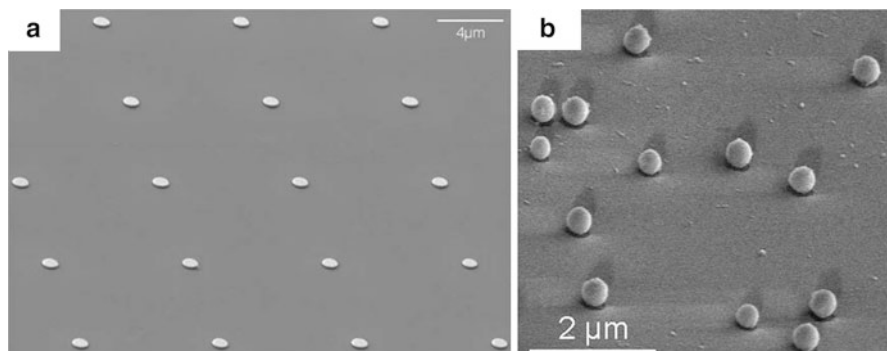
Fig. 11 SEM images of (**a**) submicron Au structures prepared by standard electron beam lithography; (**b**) Au nanoparticles collected on a glass surface after laser exposing the starting Au structure of Fig. 10a (Adapted from Ref. [77]. Reprinted with permission from Springer, Copyright (2008))

Fig. 12 Temperature dependence of the surface plasmon absorption bandwidth (normalized to SP bandwidth at 77 K) for copper nanoparticles of different sizes. The *arrows* mark the temperatures of the melting of nanoparticles (Reproduced from Ref. [84]. Reprinted with permission from the American Physical Society, Copyright (2007))
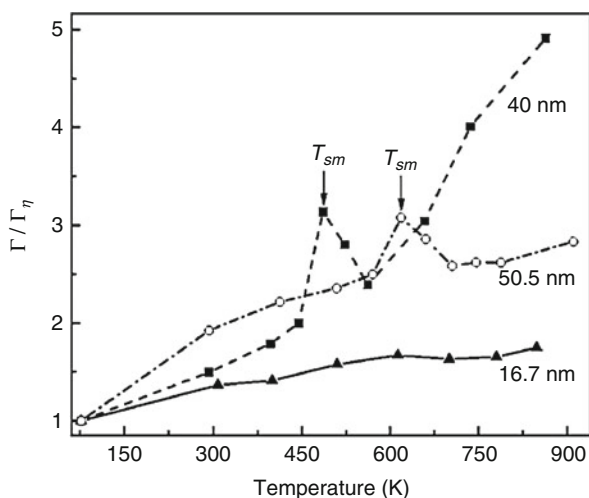
temperature dependence of the SPR absorption bandwidth for copper nanoparticles with different sizes, which is due to the increase of the frequency of the electron-phonon scattering with the increase of temperature [84].

Besides the absorption spectroscopy, the melting point depression of silver nanoparticle was identified from variations in the oscillator parameters by using in situ spectroscopic ellipsometry [85]; the melting of gold nanoparticles embedded in ice was studied by thermooptical spectroscopy [86]; the melting of Zn nanoparticles embedded in a silica matrix was monitored by a glancing incident angle X-ray diffraction (XRD) [87].

Computer Simulations

Although the experimental techniques, such as TEM observation, nanocalorimetry, and X-ray diffraction, have been established to study the melting process of nanoparticles, the understanding of this problem has not been addressed satisfactorily because it is not applicable to measure the temperature for a free-standing, mass-selected nanoparticle in vacuum. At present, computer simulation techniques, including both the molecular dynamics (MD) simulation and Monte Carlo (MC) simulation, have been proven to be powerful methods to investigate the melting behavior of single metal nanoparticles. They can provide not only adequate and accurate melting characteristics at the atomic level but also a direction of experimental analysis of nanoparticles in a larger scale.

In a MD simulation, the interactions between metal atoms are mostly employed by many atom potential models, such as embedded atom model (EAM), the glue model, tight-binding potential with a second-moment approximation (TB-SMA), and Sutton-Chen (SC) potential [88], which define the form of total energy of an N-atom system [89]. Generally, the melting behavior of the nanoparticle was monitored by the variation of the overall nanoparticle Lindemann index with respect to temperature, the variation of the individual atomic Lindemann indexes with respect to temperature, the variation of the total energy or potential energy with temperature, and specific heat capacity [90–92].

Many MD simulations have been conducted to investigate the melting behavior of pure metal nanoparticles [89, 91, 93, 94], nanowires [92, 95–99], bimetallic alloys [92, 100–102], and core-shell structures [100, 103, 104]. The melting point and heat of fusion depression are most evident from MD simulation study, and the surface atoms are subjected to premelting phenomena at temperatures below the estimated melting point of the nanoparticle systems due to the higher mobility of surface atoms. Miao et al. found that the melting temperatures of the Pd nanowire (with 1,568 atoms) of 1,200 K were lower than the simulated bulk value – 1,760 K – but higher than that of Pd cluster (with 456 atoms) at 1,090 K [97]. A quasi-liquid skin grew from the surface in the radial direction for both cluster and nanowire in the surface premelting regime [97]. Sankaranarayanan et al. reported the melting and structural evolution of bimetallic Pd-Pt nanowire with diameters ranging from 2.3 to 3.5 nm and found that the melting transition temperatures for these bimetallic nanowires are much lower than those of bulk alloys of the same composition and at least 100–200 K higher than those of nanoclusters of the same diameter, due to the different melting mechanisms between nanowires and nanoclusters [92]. The onset of surface melting of nanowire is characterized by in-plane or cross-sectional two-dimensional movement than along the axis, which is very different from the isotropic three-dimensional movement in same-diameter nanoclusters [92]. The melting behavior of Pt-Au core-shell structure was studied by Yang et al., who noticed that the increasing concentration of Pt can lead to an increase of the melting temperature of the bimetallic system [100]. In addition, the melting temperature of nanocluster on substrate was studied by MD method too [105].

Applications Related to Nanoparticle Melting Point Depression

Melting point depression is relevant to many applications of metal nanoparticles, e.g., catalyst stability, device reliability, etc. Here, they focus on two areas that are most relevant to this phenomenon, as discussed below.
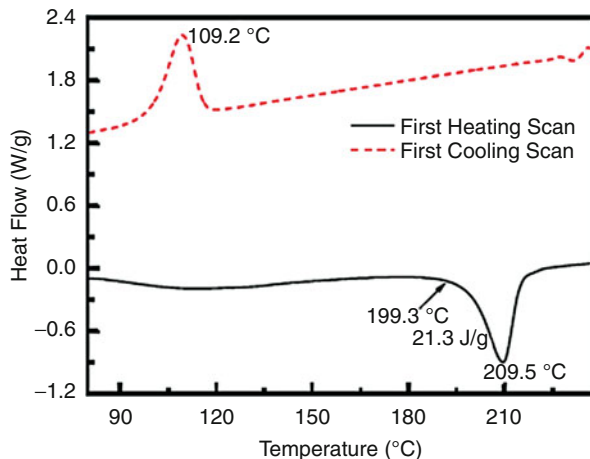
Microjoining/Nanojoining and Electronics Assembly

The most successful example of nanoparticle melting temperature depression is provided by the microjoining and nanojoining applications. Due to the requirements of the electronics miniaturization with faster operation, smaller integrated circuits, and lower cost, there is an emerging and continuous need to join nanostructures to each other, to be integrated into micro/nanoscale devices and system. Recently, the advanced microjoining and nanojoining materials have been synthesized and developed for micro/nanoelectronics assembly and packaging applications [106].

Nanosoldering has drawn great attention as a possibly significant nanojoining process in both the microelectronics industry and emerging nanoelectronics device assembly and packaging. First, due to the phasing out of toxic lead (Pb) in the present electronics industry, lead-free solder materials (e.g., SAC305-Sn/Ag/Cu alloy with bulk $T_m = 218\ °C$) have ~35 °C higher melting temperature than the eutectic Pb/Sn (37/63) solder (bulk $T_m = 183\ °C$), which increases the risk of the electrical component damage during the reflow process of electronics assembly manufacturing. The nanoscale solder (nanosolder) with smaller particle size could potentially have lower melting temperature for the same material, which provides a solution for lowering the high melting temperature of Pb-free material in the current industry. Second, the typical micron-sized solders cannot satisfy the applications of the microscale and nanoscale joining and integration. For example, novel micro/nanojoining processes are urgently needed for packaging and interconnecting in MEMS (microelectromechanical system), where individual electrical, mechanical, fluidic, and optical components need to be connected and coupled to the macroscopic external environment [75, 106].

The tin-based Pb-free nanosolders such as pure Sn, Sn/Ag, Sn/Ag/Cu, and Sn/In alloy nanostructures have been successfully synthesized [17, 20, 40, 53, 55, 107–109]. Due to the lack of thermodynamic parameters of alloy systems (material properties), in general it is difficult to conduct theoretical calculations of the melting temperature of alloy systems, and most work has been focused on experimental measurements. The melting temperature depressions from few degrees to tens of degrees have been measured by DSC in Sn/Ag, Sn/Ag/Cu, and Sn/In nanoparticle alloy systems [20, 40, 53]. However, the DSC measurement of melting temperature depression for Sn nanowire in the diameter around 50 nm and length in 5 μm was just 0.7 °C, which indicates that the melting point of nanowire in this size scale is almost the same as that of the bulk material [12]. Similarly, a 1.3 °C melting point depression was observed in Sn nanorods [17].

Jiang et al. synthesized Sn/Ag alloy nanoparticles and studied their melting point depression by the DSC measurement, as shown in Fig. 13. The result shows that the melting point of Sn/Ag alloy nanoparticles was ~209.5 °C, about 13 °C lower than that of the bulk material (222.6 °C). The onset temperature was 199.3 °C, which indicated the melting of nanoparticles. A smaller heat of fusion of the Sn/Ag alloy nanoparticle, 24.2 J/g, was measured, compared to the bulk value of 68.6 J/g [20].

Gao et al. studied the melting behavior of Sn nanowires and nanorods on Si substrate [110]. The complete melting of the Sn and Sn/Ag alloy nanosolders leads to the formation of nanoscale to microscale spherical solder balls, as shown in Fig. 14a–d. From Fig. 14b, the relatively large contact angle (greater than 90°) measured through SEM (scanning electron microscopy) image is caused by non-wetting Si substrate. Compared to the solder nanowires, the average size of the solder balls formed from nanorods was significantly smaller than that from nanowires (the average diameter of solder balls is less than 1 μm), as shown in Fig. 14d. This can attribute that (1) the volume of a single nanorod was smaller than a single nanowire and (2) the distribution of nanorods on the Si wafer when deposited was more uniform than that of the nanowires. Also, the onset melting temperature of the Sn nanowires can be as low as 190 °C with certain type of flux applied during the reflow process, which was about 40 °C lower than the melting temperature of the bulk Sn.

Koppers et al. developed Sn nanosolder pastes (20 vol% metals loading) with nanosolder particle size of 5 nm and studied their melting temperatures [108]. A four-cycle DSC measurement was applied to characterize the thermodynamic properties of the nanoparticle/flux combinations, and the results are shown in Fig. 15. The signal from the first heating cycle is dominated by reactions among the nanoparticle surfaces, surfactant, and flux, other than nanoparticle melting. The melting peak is observed with a melting onset at 153 °C during the second heating cycle. The melting temperatures and solidification temperatures increase as the nanoparticle sizes increase by coalescence of nanoparticles in each heating cycle.
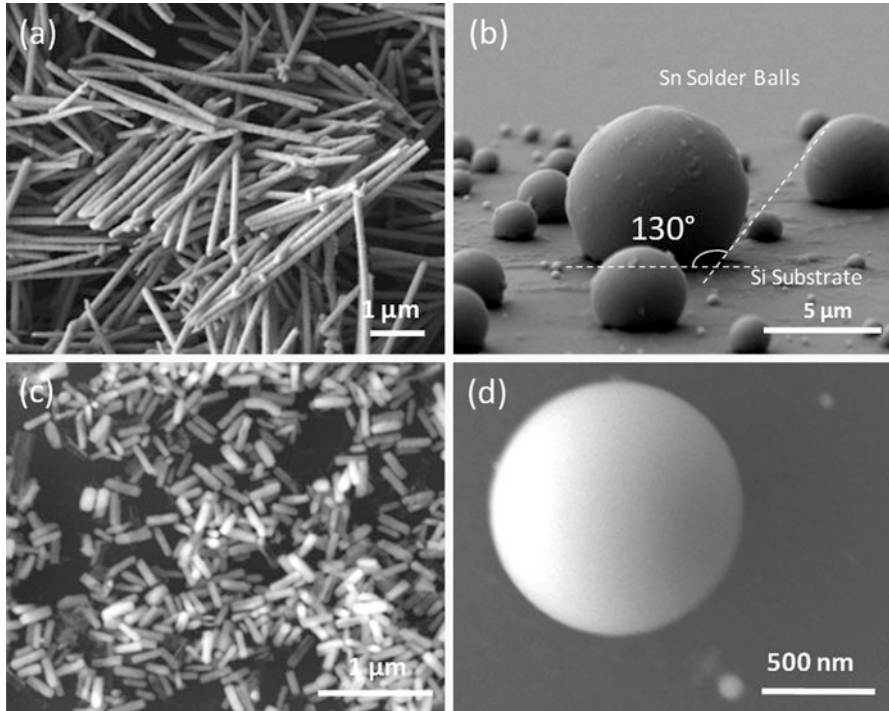
Fig. 14 Melting behavior of Sn-based nanowires and nanorods. (**a**) SEM image of Sn/Ag alloy nanowires with 50 nm diameter and 5 μm length, (**b**) microscale contact angle measurement of reflowed Sn solders on a Si wafer substrate after reflow process, (**c**) SEM image of Sn nanorods, (**d**) reflowed Sn nanorods in N_2 environment with RMA flux vapor (Adapted from Ref. [110]. Reprinted with permission from Elsevier, Copyright (2012))

Fig. 15 DSC data for a Sn nanosolder paste (nanoparticles mixed with flux). The number under each peak corresponds to the cycle number (Adapted from Ref. [108]. Reprinted with permission from Elsevier, Copyright (2012))
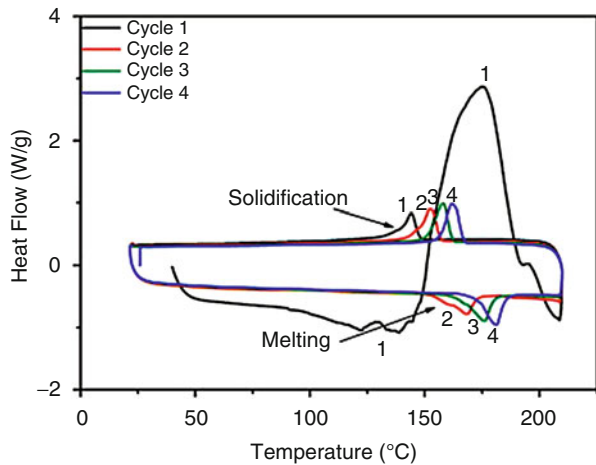
Flexible Electronics

Due to the advantages of lightweight, favorable dielectric properties, flexible electronics are increasingly being used in a number of applications. The development of electric circuit fabrication on polymer substrates, especially the high-resolution direct printing, becomes a key technique to replace the conventional vacuum deposition and photolithographic patterning methods [111]. An important issue of the flexible electronics devices is the conductive structure. Inkjet-printing process is a versatile printing technique. A major challenge in applying inkjet techniques for the printed pattern is the formulation of suitable inks. In order to be compatible with flexible substrates (e.g., polyethylene terephthalate, PET), the ink should be processed at temperatures below 150 °C or lower. Hence, one of the basic requirements for the metal-based inks is forming good electrical conductivity with low processing temperatures, such as sintering and annealing. Sintering and annealing are very simple heat treatment methods to obtain the structural transformation.

Since the melting temperature of nanoparticles depends on the particle size and material type, nanoinks consisting of metal-based nanoparticles with low melting point provide a solution for the conductive pattern formation. For high electrical conductivity purpose, gold ($\sigma = 4.42 \times 10^7 \Omega^{-1}\,m^{-1}$), silver ($\sigma = 6.3 \times 10^7 \Omega^{-1}\,m^{-1}$), copper ($\sigma = 5.96 \times 10^7 \Omega^{-1}\,m^{-1}$), and aluminum ($\sigma = 3.78 \times 10^7 \Omega^{-1}\,m^{-1}$) nanoparticles are the popular candidates as a nanoink to form printed electronics [112]. The nanoparticles were synthesized and dispersed into either organic-based (e.g., diethylene glycol) or water-based solvents, and then the nanoparticle suspension was placed in the inkjet printer with nozzles to print the pattern by drop-on-demand methods, such as thermal, piezoelectric, electrostatic, or acoustic generation of droplets [113]. After printing, the substrate will be sintered at certain temperatures in order to coalesce the nanoparticles and increase the electrical conductivity.

The sintering of nanoparticles could lead to a significant increase in electrical conductivity. Low-temperature sintering behavior of Ag nanoparticles was investigated by Moon et al. [114]. They used Ag nanoparticles of ~20 nm in diameter and sintered at 150 °C which was much lower than the bulk material melting temperature of 960 °C. Zou et al. sintered Ag nanoparticles at 250 °C under 20 MPa to bond Cu metal pieces for high-temperature electronics applications [56]. Kang et al. reported the sintering of Ag nanoparticle at room temperature with intense pulsed light (IPL) [115]. Similarly, the 5 nm Cu nanoink was printed and sintered by IPL methods [116].

Issues with Metallic Nanoparticles

Non-noble metals are usually rapidly oxidized on their surface at ambient conditions. The effect of this thermodynamically stable surface oxide structure is amplified when the particles size is down to the nanoscale. Normally, a natural oxide

layer formed on a metal surface at ambient conditions is few nanometers, which may be negligible for macroscopic materials; however, the oxide layer will significantly affect the nanoscale materials in terms of their physical and chemical properties.

For example, exposure to air or oxygen has been reported to cause a red shift of Ag nanoparticle plasmonic bands and change of surface-enhanced Raman scattering [117, 118]; the thin oxide layer (3 ~ 4 nm) on both tin nanowires and nanorods can dramatically affect their melting behavior [110]; aluminum nanoparticle with a 2 nm thick alumina shell has higher melting temperature predicted by the Gibbs-Thomson equation, due to the pressure generated by the Al core [51]; and the melting temperature of Zn nanoparticle confined to the ZnO shell is 1–2° less than that of bulk Zn [52].

For the nanomaterial application, the oxide layer will affect the processes from many perspectives. For example, copper is a good alternative material as it is highly conductive and much cheaper than Au and Ag. However, the surface oxide layer on the Cu nanoparticles normally results in a higher processing temperature (e.g., sintering/annealing) and lower electrical conductivity [57]. On the other hand, the surface oxide will result in the difficulty of measurement accuracy, such as the DSC measurement. The experimental measurement of melting temperature by DSC was higher than the theoretical calculated result, which is due to the surface oxidation during the nanoparticle synthesis [53].

In addition, nanoparticle agglomeration is another significant issue to affect the measurement and applications. The severe nanoparticle agglomeration will reduce the overall surface-to-volume ratio and hence reduce or even completely lose the surface active properties.

Conclusion

Both the theoretical and experimental investigations proved the size-dependent melting temperature depression of metallic nanoparticles. This solid to liquid phase transition in nanoparticle is more complex than macroscopic scale substance. The nature of nanoparticle melting behavior can be revealed with strong theoretical analysis. Many models indicate that nanoparticle surfaces melt at a lower temperature than that of the interiors with two-phase coexistence. The thermodynamic models can be modified and applied to understand the melting behavior of nanoparticles in different shapes. The available tools such as DSC, nanocalorimeter, TEM, laser-based methods, and optical instruments can provide observable results of melting temperature of nanoparticles with a high degree of accuracy. As the particle size decreases, the accurate melting temperature measurement becomes more difficult due to various issues, including nanoparticle agglomeration and surface oxidation. The lower melting temperature of metallic nanoparticle could contribute to the nanoscale to microscale joining and interconnection for the advanced microelectronics/nanoelectronics devices and flexible electronics assembly.

References

1. F.E. Kruis, H. Fissan, A. Peled, Synthesis of nanoparticles in the gas phase for electronic, optical and magnetic applications—a review. J. Aerosol Sci. **29**, 511 (1998)
2. M.T. Swihart, Vapor-phase synthesis of nanoparticles. Curr. Opin. Colloid Interface Sci. **8**, 127 (2003)
3. B.L. Cushing, V.L. Kolesnichenko, C.J. O'Connor, Recent advances in the liquid-phase syntheses of inorganic nanoparticles. Chem. Rev. **104**, 3893 (2004)
4. G. Caruntu, D. Caruntu, C.J. O'Connor, *Liquid-Phase Synthesis of Inorganic Nanoparticles. Encyclopedia of Inorganic Chemistry*, Wiley, Chichester (2009)
5. C.L. DeCastro, B.S. Mitchell, *"Nanoparticles from mechanical attrition"*, Synthesis, functionalization, and surface treatment of nanoparticles, American Scientific Publishers, Chapter 1, 1–15 (2003)
6. F. Mafune, J.-y. Kohno, Y. Takeda, T. Kondow, H. Sawabe, Formation and size control of silver nanoparticles by laser ablation in aqueous solution. J. Phys. Chem. B **104**, 9111 (2000)
7. Y. Wu, P. Yang, Direct observation of vapor-liquid-solid nanowire growth. J. Am. Chem. Soc. **123**, 3165 (2001)
8. Y. Xia, P. Yang, Y. Sun, Y. Wu, B. Mayers, B. Gates, Y. Yin, F. Kim, H. Yan, One-dimensional nanostructures: synthesis, characterization, and applications. Adv. Mater. **15**, 353 (2003)
9. N.R. Jana, L. Gearheart, C.J. Murphy, Evidence for seed-mediated nucleation in the chemical reduction of gold salts to gold nanoparticles. Chem. Mater. **13**, 2313 (2001)
10. I. Capek, Preparation of metal nanoparticles in water-in-oil (w/o) microemulsions. Adv. Colloid Interface Sci. **110**(49) (2004)
11. B.M. Quinn, C. Dekker, S.G. Lemay, Electrodeposition of noble metal nanoparticles on carbon nanotubes. J. Am. Chem. Soc. **127**, 6146 (2005)
12. F. Gao, S. Mukherjee, Q. Cui, Z. Gu, Synthesis, characterization, and thermal properties of nanoscale lead-free solders on multisegmented metal nanowires. J. Phys. Chem. C **113**, 9546 (2009)
13. Y. Yang, S. Matsubara, L. Xiong, T. Hayakawa, M. Nogami, Solvothermal synthesis of multiple shapes of silver nanoparticles and their SERS properties. J. Phys. Chem. C **111**, 9095 (2007)
14. M. Grzelczak, J. Pérez-Juste, P. Mulvaney, L.M. Liz-Marzán, Shape control in gold nanoparticle synthesis. Chem. Soc. Rev. **37**, 1783 (2008)
15. H. Yoo, J.E. Millstone, S. Li, J.-W. Jang, W. Wei, J. Wu, G.C. Schatz, C.A. Mirkin, Core — shell triangular bifrustums. Nano Lett. **9**, 3038 (2009)
16. W. Niu, W. Zhang, S. Firdoz, X. Lu, Controlled synthesis of palladium concave nanocubes with Sub-10-nanometer edges and corners for tunable plasmonic property. Chem. Mater **26**, 2180 (2014) doi: 10.1021/cm500210u
17. Q. Cui, K. Rajathurai, W. Jia, X. Li, F. Gao, Y. Lei, Z. Gu, Synthesis of single crystalline tin nanorods and their application as nanosoldering materials. J. Phys. Chem. C **114**, 21938 (2010)
18. D.H.M. Dam, J.H. Lee, P.N. Sisco, D.T. Co, M. Zhang, M.R. Wasielewski, T.W. Odom, Direct observation of nanoparticle–cancer cell nucleus interactions. ACS Nano **6**, 3318 (2012)
19. F. Caruso, R.A. Caruso, H. Möhwald, Nanoengineering of inorganic and hybrid hollow spheres by colloidal templating. Science **282**, 1111 (1998)
20. H. Jiang, K.-s. Moon, F. Hua, C. Wong, Synthesis and thermal and wetting properties of tin/silver alloy nanoparticles for low melting point lead-free solders. Chem. Mater. **19**, 4482 (2007)

21. H. Song, F. Kim, S. Connor, G.A. Somorjai, P. Yang, Pt nanocrystals: shape control and langmuir − blodgett monolayer formation. J. Phys. Chem. B **109**, 188 (2004)

22. W. Ni, Z. Yang, H. Chen, L. Li, J. Wang, Coupling between molecular and plasmonic resonances in freestanding dye − gold nanorod hybrid nanostructures. J. Am. Chem. Soc. **130**, 6692 (2008)

23. J. Sarkar, G.G. Khan, A. Basumallick, Nanowires: properties, applications and synthesis via porous anodic aluminium oxide template. Bull. Mater. Sci. **30**, 271 (2007)

24. E. Roduner, Size matters: why nanomaterials are different. Chem. Soc. Rev. **35**, 583 (2006)

25. P. Buffat, J.P. Borel, Size effect on the melting temperature of gold particles. Phys. Rev. A **13**, 2287 (1976)

26. C.A. Johnson, Generalization of the Gibbs-Thomson equation. Surf. Sci. **3**, 429 (1965)

27. K. Nanda, Size-dependent melting of nanoparticles: hundred years of thermodynamic model. Pramana **72**, 617 (2009)

28. M. Zhang, M.Y. Efremov, F. Schiettekatte, E. Olson, A. Kwan, S. Lai, T. Wisleder, J. Greene, L. Allen, Size-dependent melting point depression of nanostructures: nanocalorimetric measurements. Phys. Rev. B **62**, 10548 (2000)

29. P. Pawlow, Über die abhängigkeit des schmelzpunktes von der oberflächenenergie eines festen körpers. Z. Phys. Chem. **65**, 1 (1909)

30. K.K. Nanda, S.N. Sahu, S.N. Behera, Liquid-drop model for the size-dependent melting of low-dimensional systems. Phys. Rev. A **66**, 013208 (2002)

31. C.Q. Sun, Y. Wang, B.K. Tay, S. Li, H. Huang, Y.B. Zhang, Correlation between the melting point of a nanosolid and the cohesive energy of a surface atom. J. Phys. Chem. B **106**, 10701 (2002)

32. H. Reiss, I.B. Wilson, The effect of surface on melting point. J. Colloid Sci. **3**, 551 (1948)

33. W. Qi, M. Wang, Size and shape dependent melting temperature of metallic nanoparticles. Mater. Chem. Phys. **88**, 280 (2004)

34. S.L. Lai, J.R.A. Carlsson, L.H. Allen, Melting point depression of Al clusters generated during the early stages of film growth: Nanocalorimetry measurements. Appl. Phys. Lett. **72**, 1098 (1998)

35. P. Antoniammal, D. Arivuoli, Size and shape dependence on melting temperature of gallium nitride nanoparticles. J. Nanomater. **2012**(8) (2012)

36. R.R. Vanfleet, J.M. Mochel, Thermodynamics of melting and freezing in small particles. Surf. Sci. **341**, 40 (1995)

37. H. Reiss, P. Mirabel, R.L. Whetten, Capillarity theory for the "coexistence" of liquid and solid clusters. J. Phys. Chem. **92**, 7241 (1988)

38. P. Couchman, W. Jesser, Thermodynamic theory of size dependence of melting temperature in metals. Nature **269**, 481 (1977)

39. A. Barybin, V. Shapovalov, Modification of Pawlow's thermodynamical model for the melting of small single-component particles. J. Appl. Phys. **109**, 034303 (2011)

40. G. Guisbiers, M. Wautelet, Size, shape and stress effects on the melting temperature of nano-polyhedral grains on a substrate. Nanotechnology **17**, 2008 (2006)

41. H.M. Lu, P.Y. Li, Z.H. Cao, X.K. Meng, Size-, Shape-, and dimensionality-dependent melting temperatures of nanocrystals. J. Phys. Chem. C **113**, 7598 (2009)

42. D.K. Sar, P. Nayak, K.K. Nanda, Thermodynamic model for the size-dependent melting of prism-shaped nanoparticles. Phys. Lett. A **372**, 4627 (2008)

43. M. Attarian Shandiz, A. Safaei, S. Sanjabi, Z.H. Barber, Modeling size dependence of melting temperature of metallic nanoparticles. J. Phys. Chem. Solid **68**, 1396 (2007)

44. S. Lai, J. Guo, V. Petrova, G. Ramanath, L. Allen, Size-dependent melting properties of small tin particles: nanocalorimetric measurements. Phys. Rev. Lett. **77**, 99 (1996)

45. C. Chen, J.-G. Lee, K. Arakawa, H. Mori, In situ observations of crystalline-to-liquid and crystalline-to-gas transitions of substrate-supported Ag nanoparticles. Appl. Phys. Lett. **96**, 253104 (2010)

46. J. Lee, T. Tanaka, J. Lee, H. Mori, Effect of substrates on the melting temperature of gold nanoparticles. Calphad **31**, 105 (2007)
47. P. Gill, T.T. Moghadam, B. Ranjbar, Differential scanning calorimetry techniques: applications in biology and nanoscience. J. Biomol. Tech. **21**, 167 (2010)
48. A. Jeziorny, Parameters characterizing the kinetics of the non-isothermal crystallization of poly (ethylene terephthalate) determined by DSC. Polymer **19**, 1142 (1978)
49. P.J. Haines, F.W. Wilburn, Differential thermal analysis and differential scanning calorimetry, in *Thermal Methods of Analysis* (Springer, The Netherlands, 1995), pp. 63–122
50. R.L. Danley, New heat flux DSC measurement technique. Thermochimica Acta. **395**, 201 (2002)
51. V.I. Levitas, M.L. Pantoya, G. Chauhan, I. Rivero, Effect of the alumina shell on the melting temperature depression for aluminum nanoparticles. J. Phys. Chem. C **113**, 14088 (2009)
52. L. Gunawan, G.P. Johari, Specific heat, melting, crystallization, and oxidation of zinc nanoparticles and their transmission electron microscopy studies. J. Phys. Chem. C **112**, 20159 (2008)
53. J. Hongjin, M. Kyoung-Sik, F. Hua, C.P. Wong, *Thermal properties of tin/silver alloy nanoparticles for low temperature lead-free interconnect technology*. in Electronic Components and Technology Conference. ECTC '07. Proceedings. 57th. 54 (2007)
54. N.H. Kim, J.-Y. Kim, K.J. Ihn, Preparation of silver nanoparticles having low melting temperature through a new synthetic process without solvent. J. Nanosci. Nanotechnol. **7**, 3805 (2007)
55. T.T. Bao, Y. Kim, J. Lee, J.-G. Lee, Preparation and thermal analysis of Sn-Ag nano solders. Mater. Trans. **51**, 2145 (2010)
56. G. Zou, J. Yan, F. Mu, A. Wu, J. Ren, A. Hu, Y. Zhou, Low temperature bonding of Cu metal through sintering of Ag nanoparticles for high temperature electronic application. Open Surf. Sci. J. **3**, 70 (2011)
57. S. Jeong, K. Woo, D. Kim, S. Lim, J.S. Kim, H. Shin, Y. Xia, J. Moon, Controlling the thickness of the surface oxide layer on Cu nanoparticles for the fabrication of conductive structures by ink jet printing. Adv. Funct. Mater. **18**, 679 (2008)
58. H. Jiang, K.-S. Moon, H. Dong, F. Hua, C.P. Wong, Size-dependent melting properties of tin nanoparticles. Chem. Phys. Lett. **429**, 492 (2006)
59. S.L. Lai, G. Ramanath, L.H. Allen, P. Infante, Z. Ma, High-speed (10^4 °C/s) scanning microcalorimetry with monolayer sensitivity (J/m^2). Appl. Phys. Lett. **67**, 1229 (1995)
60. M. Schmidt, R. Kusche, B. von Issendorff, H. Haberland, Irregular variations in the melting point of size-selected atomic clusters. Nature **393**, 238 (1998)
61. M. Takagi, Electron-diffraction study of liquid-solid transition of thin metal films. J. Physical Soc. Japan **9**, 359 (1954)
62. C.R.M. Wronski, The size dependence of the melting point of small particles of tin. Br. J. Appl. Phys. **18**, 1731 (1967)
63. M. Blackman, A. Curzon, *Structure and Properties of Thin Films* (Wiley, New York, 1959), p. 217
64. C. Coombes, The melting of small particles of lead and indium. J. Phys. F: Met. Phys. **2**, 441 (1972)
65. N.T. Gladkich, R. Niedermayer, K. Spiegel, Nachweis großer schmelzpunktserniedrigungen bei dünnen metallschichten. *Physica status solidi* (b). **15**, 181 (1966)
66. R. Berman, A. Curzon, The size dependence of the melting point of small particles of indium. Can. J. Phys. **52**, 923 (1974)
67. M. José-Yacamán, C. Gutierrez-Wing, M. Miki, D.Q. Yang, K.N. Piyakis, E. Sacher, Surface diffusion and coalescence of mobile metal nanoparticles. J. Phys. Chem. B **109**, 9703 (2005)
68. B. Liu, Y. Bando, M. Wang, C. Zhi, X. Fang, C. Tang, M. Mitome, D. Golberg, Electron-beam irradiation induced conductivity in ZnS nanowires as revealed by in situ transmission electron microscope. J. Appl. Phys. **106**, 034302 (2009)

69. Z.W. Pan, Z.R. Dai, Z.L. Wang, Lead oxide nanobelts and phase transformation induced by electron beam irradiation. Appl. Phys. Lett. **80**, 309 (2002)

70. L. Marks, P. Ajayan, J. Dundurs, Quasi-melting of small particles. Ultramicroscopy **20**, 77 (1986)

71. P.M. Ajayan, L.D. Marks, Experimental evidence for quasimelting in small particles. Phys. Rev. Lett. **63**, 279 (1989)

72. F. Gao, Z. Liu, G. Zhou, J.C. Yang, Z. Gu, Fast diffusion and void formation in a Two-segment copper-Tin lead-free nanowire system with one-dimensional confinement. Sci. Adv. Mater. **4**, 881 (2012)

73. Z.L. Wang, J.M. Petroski, T.C. Green, M.A. El-Sayed, Shape transformation and surface melting of cubic and tetrahedral platinum nanocrystals. J. Phys. Chem. B **102**, 6145 (1998)

74. F. Baletto, R. Ferrando, Structural properties of nanoclusters: energetic, thermodynamic, and kinetic effects. Rev. Mod. Phys. **77**, 371 (2005)

75. M.M. Alvarez, J.T. Khoury, T.G. Schaaff, M.N. Shafigullin, I. Vezmar, R.L. Whetten, Optical absorption spectra of nanocrystal gold molecules. J. Phys. Chem. B **101**, 3706 (1997)

76. A. Habenicht, M. Olapinski, F. Burmeister, P. Leiderer, J. Boneberg, Jumping nanodroplets. Science **309**, 2043 (2005)

77. J. Boneberg, A. Habenicht, D. Benner, P. Leiderer, M. Trautvetter, C. Pfahler, A. Plettl, P. Ziemann, Jumping nanodroplets: a new route towards metallic nano-particles. Appl. Phys. A **93**, 415 (2008)

78. S. Inasawa, M. Sugiyama, Y. Yamaguchi, Laser-induced shape transformation of gold nanoparticles below the melting point: the effect of surface melting. J. Phys. Chem. B **109**, 3104 (2005)

79. J.H. Hodak, A. Henglein, M. Giersig, G.V. Hartland, Laser-induced inter-diffusion in AuAg core − shell nanoparticles. J. Phys. Chem. B **104**, 11708 (2000)

80. S.J. Tan, M.J. Campolongo, D. Luo, W. Cheng, Building plasmonic nanostructures with DNA. Nat. Nano. **6**, 268 (2011)

81. S. Link, M.A. El-Sayed, Spectral properties and relaxation dynamics of surface plasmon electronic oscillations in gold and silver nanodots and nanorods. J. Phys. Chem. B **103**, 8410 (1999)

82. S. Link, C. Burda, B. Nikoobakht, M.A. El-Sayed, How long does it take to melt a gold nanorod?: a femtosecond pump–probe absorption spectroscopic study. Chem. Phys. Lett. **315**, 12 (1999)

83. K. Yamada, Y. Tokumoto, T. Nagata, F. Mafuné, Mechanism of laser-induced size-reduction of gold nanoparticles as studied by nanosecond transient absorption spectroscopy. J. Phys. Chem. B **110**, 11751 (2006)

84. O.A. Yeshchenko, I.M. Dmitruk, A.A. Alexeenko, A.M. Dmytruk, Size-dependent melting of spherical copper nanoparticles embedded in a silica matrix. Phys. Rev. B **75**, 085434 (2007)

85. S.A. Little, T. Begou, R.W. Collins, S. Marsillac, Optical detection of melting point depression for silver nanoparticles via in situ real time spectroscopic ellipsometry. Appl. Phys. Lett. **100**, 051107 (2012)

86. H.H. Richardson, Z.N. Hickman, A.O. Govorov, A.C. Thomas, W. Zhang, M.E. Kordesch, Thermooptical properties of gold nanoparticles embedded in Ice: characterization of heat generation and melting. Nano Lett. **6**, 783 (2006)

87. H. Amekura, M. Tanaka, Y. Katsuya, H. Yoshikawa, H. Shinotsuka, S. Tanuma, M. Ohnuma, Y. Matsushita, K. Kobayashi, C. Buchal, S. Mantl, N. Kishimoto, Melting of Zn nanoparticles embedded in SiO_2 at high temperatures: effects on surface plasmon resonances. Appl. Phys. Lett. **96**, 023110 (2010)

88. B.D. Todd, R.M. Lynden-Bell, Surface and bulk properties of metals modelled with Sutton-Chen potentials. Surf. Sci. **281**, 191 (1993)

89. J.-H. Shim, B.-J. Lee, Y.W. Cho, Thermal stability of unsupported gold nanoparticle: a molecular dynamics study. Surf. Sci. **512**, 262 (2002)

90. E.C. Neyts, A. Bogaerts, Numerical study of the size-dependent melting mechanisms of nickel nanoclusters. J. Phys. Chem. C **113**, 2771 (2009)

91. S. Alavi, D.L. Thompson, Molecular dynamics simulations of the melting of aluminum nanoparticles. J. Phys. Chem. A **110**, 1518 (2005)

92. S.K.R.S. Sankaranarayanan, V.R. Bhethanabotla, B. Joseph, Molecular dynamics simulation study of the melting and structural evolution of bimetallic Pd-Pt nanowires. Phys. Rev. B **74**, 155441 (2006)

93. F. Delogu, Structural and energetic properties of unsupported Cu nanoparticles from room temperature to the melting point: Molecular dynamics simulations. Phys. Rev. B **72**, 205418 (2005)

94. Y. Shibuta, T. Suzuki, A molecular dynamics study of the phase transition in bcc metal nanoparticles. J. Chem. Phys. **129**, 144102 (2008)

95. G. Bilalbegović, Structures and melting in infinite gold nanowires. Solid State Commun. **115**, 73 (2000)

96. Y.-H. Wen, Z.-Z. Zhu, R. Zhu, G.-F. Shao, Size effects on the melting of nickel nanowires: a molecular dynamics study. Physica E **25**, 47 (2004)

97. L. Miao, V.R. Bhethanabotla, B. Joseph, Melting of Pd clusters and nanowires: a comparison study using molecular dynamics simulation. Phys. Rev. B **72**, 134109 (2005)

98. J. Wang, X. Chen, G. Wang, B. Wang, W. Lu, J. Zhao, Melting behavior in ultrathin metallic nanowires. Phys. Rev. B **66**, 085408 (2002)

99. B. Wang, G. Wang, X. Chen, J. Zhao, Melting behavior of ultrathin titanium nanowires. Phys. Rev. B **67**, 193403 (2003)

100. Z. Yang, X. Yang, Z. Xu, Molecular dynamics simulation of the melting behavior of Pt-Au nanoparticles with core-shell structure. J. Phys. Chem. C **112**, 4937 (2008)

101. S.K.R.S. Sankaranarayanan, V.R. Bhethanabotla, B. Joseph, Molecular dynamics simulation study of phase transformations in transition bimetallic nanowires. J. Phys. Chem. C **111**, 2430 (2007)

102. H.B. Liu, U. Pal, J.A. Ascencio, Thermodynamic stability and melting mechanism of bimetallic Au − Pt nanoparticles. J. Phys. Chem. C **112**, 19173 (2008)

103. Z. Kuntová, G. Rossi, R. Ferrando, Melting of core-shell Ag-Ni and Ag-Co nanoclusters studied via molecular dynamics simulations. Phys. Rev. B **77**, 205431 (2008)

104. T. Shibata, B.A. Bunker, Z. Zhang, D. Meisel, C.F. Vardeman, J.D. Gezelter, Size-dependent spontaneous alloying of Au − Ag nanoparticles. J. Am. Chem. Soc. **124**, 11989 (2002)

105. F. Ding, A. Rosen, S. Curtarolo, K. Bolton, Modeling the melting of supported clusters. Appl. Phys. Lett. **88**, 133110 (2006)

106. Q. Cui, F. Gao, S. Mukherjee, Z. Gu, Joining and interconnect formation of nanowires and carbon nanotubes for nanoelectronics and nanosystems. Small **5**, 1246 (2009)

107. C. Zou, Y. Gao, B. Yang, Q. Zhai, Synthesis and DSC study on Sn3.5Ag alloy nanoparticles used for lower melting temperature solder. J. Mater. Sci. Mater. Electron. **21**(868) (2010)

108. J.P. Koppes, K.A. Grossklaus, A.R. Muza, R.R. Revur, S. Sengupta, A. Rae, E.A. Stach, C.A. Handwerker, Utilizing the thermodynamic nanoparticle size effects for low temperature Pb-free solder. Mater. Sci. Eng. B **177**, 197 (2012)

109. Y. Shu, K. Rajathurai, F. Gao, Q. Cui, Z. Gu, Synthesis and thermal properties of low melting point tin/indium (Sn/In) lead-free nanosolders and their melting behavior in a Vapor Flux. J. Alloys Comp. **626**, 391 (2014)

110. F. Gao, K. Rajathurai, Q. Cui, G. Zhou, I. NkengforAcha, Z. Gu, Effect of surface oxide on the melting behavior of lead-free solder nanowires and nanorods. Appl. Surf. Sci. **258**, 7507 (2012)

111. K. Jain, M. Klosner, M. Zemel, S. Raghunandan, Flexible electronics and displays: high-resolution, roll-to-roll, projection lithography and photoablation processing technologies for high-throughput production. Proc. IEEE. **93**, 1500 (2005)

112. A. Kamyshny, J. Steinke, S. Magdassi, Metal-based inkjet inks for printed electronics. Open Appl. Phys. J. **4**, 19 (2011)

113. A. Hudd, Inkjet printing technologies, in *The Chemistry of Inkjet Inks* (World Scientific, New Jersey/London/Singapore, 2010), p. 3
114. K.-S. Moon, H. Dong, R. Maric, S. Pothukuchi, A. Hunt, Y. Li, C.P. Wong, Thermal behavior of silver nanoparticles for low-temperature interconnect applications. J. Electron. Mater. **34**, 168 (2005)
115. J. Kang, J. Ryu, H. Kim, H. Hahn, Sintering of inkjet-printed silver nanoparticles at room temperature using intense pulsed light. J. Electron. Mater. **40**, 2268 (2011)
116. H.-S. Kim, S. Dhage, D.-E. Shim, H.T. Hahn, Intense pulsed light sintering of copper nanoink for printed electronics. Appl. Phys. A **97**, 791 (2009)
117. A. Henglein, Colloidal silver nanoparticles: photochemical preparation and interaction with O_2, CCl_4, and some metal ions. Chem. Mater. **10**, 444 (1998)
118. Y. Han, R. Lupitskyy, T.-M. Chou, C.M. Stafford, H. Du, S. Sukhishvili, Effect of oxidation on surface-enhanced Raman scattering activity of silver nanoparticles: a quantitative correlation. Anal. Chem. **83**, 5873 (2011)